# Evaluation of the Operational Multiscale Environment Model with Grid Adaptivity against the European Tracer Experiment

ZAFER BOYBEYI, NASH'AT N. AHMAD, DAVID P. BACON, THOMAS J. DUNN, MARY S. HALL, PIUS C. S. LEE, R. ANANTHAKRISHNA SARMA, AND TIM R. WAIT

*Center for Atmospheric Physics, Science Applications International Corporation, McLean, Virginia*

(Manuscript received 16 August 2000, in final form 5 March 2001)

ABSTRACT

The Operational Multiscale Environment Model with Grid Adaptivity (OMEGA) is a multiscale nonhydrostatic atmospheric simulation system based on an adaptive unstructured grid. The basic philosophy behind the OMEGA development has been the creation of an operational tool for real-time aerosol and gas hazard prediction. The model development has been guided by two basic design considerations in order to meet the operational requirements: 1) the application of an unstructured dynamically adaptive mesh numerical technique to atmospheric simulation, and 2) the use of embedded atmospheric dispersion algorithms. An important step in proving the utility and accuracy of OMEGA is the full-scale testing of the model using simulations of real-world atmospheric events and qualitative as well as quantitative comparisons of the model results with observations. The main objective of this paper is to provide a comprehensive evaluation of OMEGA against a major dispersion experiment in operational mode. Therefore, OMEGA was run to create a 72-h forecast for the first release period (23–26 October 1994) of the European Tracer Experiment (ETEX). The predicted meteorological and dispersion fields were then evaluated against both the atmospheric observations and the ETEX dispersion measurements up to 60 h after the start of the release. In general, the evaluation showed that the OMEGA dispersion results were in good agreement in the position, shape, and extent of the tracer cloud. However, the model prediction indicated that there was a limited spreading of the predictions around the measurements with a small tendency to underestimate the concentration values.

## 1. Introduction

During the past two decades there has been growing concern about estimating the long-range dispersion of pollutants over mesoscale travel distances between 20 and 2000 km (e.g., Brost et al. 1988; Moran and Pielke 1996). This concern has been motivated by relatively new environmental problems such as regional-scale acidic deposition and ozone episodes, the multicountry radionuclide contamination experienced during the Chernobyl nuclear disaster, the smoke plumes from the Kuwaiti oil and gas well fires, and Indonesian biomass burning. These problems and their consequences are truly international in scope. As our world increasingly depends on sophisticated technologies, our ability to monitor and predict the environmental and health impact of natural and anthropogenic hazardous phenomena is becoming ever more important. Therefore, emergency response systems have been developed and directed (e.g., Sullivan et al. 1993; Byun and Ching 1999) to prevent, avoid, or mitigate any impact of the hazardous materials to humans, animals, vegetation, or ecosystems. In general, emergency response can be provided in two ways: 1) diagnosis of what has happened through measurement of the concentration of hazardous material, and 2) prediction of the concentration of hazardous material.

The Operational Multiscale Environment Model with Grid Adaptivity (OMEGA) is a multiscale nonhydrostatic atmospheric simulation system with an unstructured dynamically adaptive grid that permits spatial resolutions ranging from 100 down to 1 km (Bacon et al. 2000). The basic philosophy behind the OMEGA development has been the creation of an operational tool for real-time aerosol and gas hazard prediction. The model development has been guided by two basic design considerations in order to meet the operational requirements: 1) the application of an unstructured dynamically adaptive mesh numerical technique to atmospheric simulation, and 2) the use of embedded atmospheric dispersion algorithms. In addition, as an operational tool, OMEGA was constructed using the maximum amount of automation in model configuration, data ingest, data quality control, data assimilation, grid generation, model operation, and postprocessing. The resulting modeling system is capable of rapid reconfiguration for operation anywhere in the world, with automatic linkage

*Corresponding author address*: Zafer Boybeyi, Center for Atmospheric Physics, SAIC, M/S 2-3-1, 1710 SAIC Dr., McLean, VA 22102.
E-mail: boybeyi@apo.saic.com

to baseline datasets and real-time meteorological data feeds. An important step in proving the utility and accuracy of OMEGA involves the full-scale testing of the system using simulations of real-world atmospheric conditions and qualitative as well as quantitative comparisons of the model results with observations.

Motivated by the Chernobyl accident, the European Tracer Experiment (ETEX) was conducted to evaluate and improve real-time continental-scale forecasting of meteorological and hazardous material air concentration fields (Nodop et al. 1998; van Dop et al. 1998). ETEX represented a large-scale endeavor from many points of view. Seventeen European countries were involved in the tracer experiment, with 168 ground-level sampling locations distributed over their territories in western and eastern Europe. About 28 organizations participated in the model evaluation exercise with about 49 models (e.g., Nasstrom and Pace 1998; Ryall and Maryon 1998; Langner et al. 1998; Glaab et al. 1998). The model evaluations and intercomparisons were done in two phases: a real-time study and a postexperiment study called the Atmospheric Transport Model Evaluation Study II (ATMES II; Girardi et al. 1997). During the real-time phase a perfluorocarbon tracer gas was released from Monterfil in northwestern France. Participating modeling groups with access to real-time meteorological data then made predictions, in a simulated emergency response mode, of the concentration of a tracer gas at the 168 ground-level sampling locations. In the ATMES II postexperiment study, modeling groups were asked to make the same predictions using a common source of meteorological data fields from the European Centre for Medium-Range Weather Forecasts (ECMWF), without the time restrictions of the real-time phase. Two separate ETEX tracer releases and experiment periods were used during the experiment. The first of these periods (23–26 October 1994) was used for this study.

This field program provides a unique opportunity for testing atmospheric long-range transport models against a controlled large-scale diffusion experiment. The main objective of this paper is to provide a comprehensive evaluation of OMEGA against a major dispersion experiment in operational mode. Therefore, OMEGA was run to create a 72-h forecast for the first release period (23–26 October 1994) of ETEX. The predicted meteorological and dispersion fields were then compared with the atmospheric observations and the ETEX dispersion measurements. The results indicated that OMEGA, as an operational hazard prediction system, performed well as compared with the observations.

## 2. A brief description of OMEGA

The basic features of OMEGA are provided in Table 1 and are discussed in detail by Bacon et al. (2000). A brief description of OMEGA can also be found in Bacon et al. (1996), Boybeyi et al. (1996), and Sarma et al. (1999). OMEGA is a fully nonhydrostatic, three-dimensional prognostic model. It is based on an unstructured dynamically adaptive triangular prism grid that is referenced to a rotating Cartesian coordinate system. The model uses a finite-volume flux-based numerical advection algorithm derived from Smolarkiewicz (1984). OMEGA also contains a Lagrangian dispersion algorithm embedded into the model. As part of the real-time operational requirement, much automation was implemented into the OMEGA system. This resulted in the creation of a highly automated grid generator, an automated meteorological and surface data assimilation system, and a user-friendly X-windows and Motif-based graphical user interface and graphic postprocessors.

TABLE 1. An overview of OMEGA.

| | |
|---|---|
| Governing equations | 3D fully nonhydrostatic |
| Grid structure | Unstructured triangular prisms |
| Grid adaptivity | Both static and dynamic grid adaptation |
| Coordinate system | Rotating Cartesian coordinates |
| Numeric | Finite volume |
| PBL | Treated as viscous sublayer, surface layer, and transition layer |
| Turbulence closure | 1.5-order turbulent kinetic energy closure |
| Cumulus parameterization | Modified Kuo and Kain–Fritsch schemes |
| Microphysics | Extensive bulk-water |
| Radiation | Shortwave absorption by water vapor and longwave emissivities of water vapor and carbon dioxide |
| Lower boundary | Based on Monin–Obukhov similarity theory |
| Upper boundary | Rigid, free-slip surface |
| Lateral boundaries | Radiative and large-scale nudging boundary condition |
| Initialization | Based on 4D data assimilation |
| Dispersion | Lagrangian aerosol dispersion algorithm |

### *a. The OMEGA grid structure*

An important feature of OMEGA is its unstructured grid. OMEGA is based on a triangular prism computational mesh that is unstructured in the horizontal dimension and structured in the vertical (Fig. 1). The unstructured grid in the horizontal dimension enables the model to increase local resolution to better capture topography or the important physical features of atmospheric circulation. The unstructured triangular grid methodology requires the calculation of the normal to each face in order to estimate the flux across the face. Therefore, there is no benefit from orienting the grid in any particular fashion, so long as the numerical resolution is sufficient to evaluate the critical fluxes. This leads to a natural separation between the coordinate system for the fundamental equation set and the grid structure. The coordinate system can be as simple as possible (such as Cartesian) while the grid structure, in this coordinate system, is extremely complex. OMEGA uses

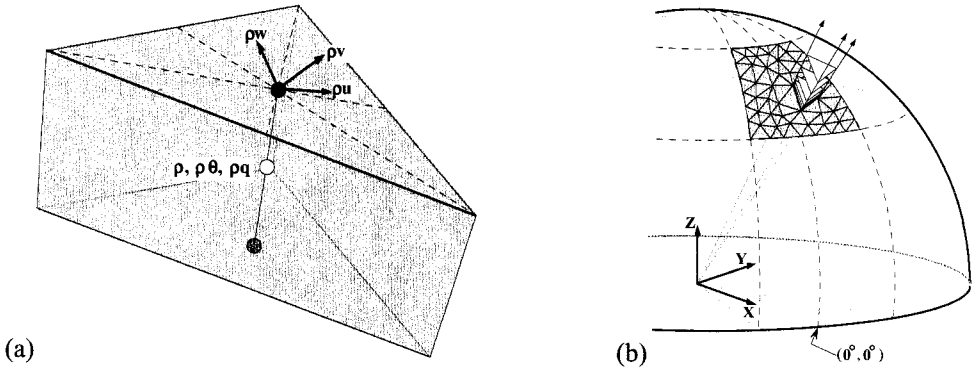


FIG. 1. The OMEGA grid structure: (a) an OMEGA grid element, and (b) the coordinate system and vertical alignment of the grid.

a rotating Cartesian coordinate system, but the grid structure is terrain-following.

Figure 1b shows the rotating Cartesian coordinate system in which the origin is the center of the earth, the $z$ axis passes through the North Pole, the $x$ axis passes through the intersection of the equator and the prime meridian, and the $y$ axis is orthogonal to both. In this coordinate frame, the equations of motion are in their simplest possible form (without going into a nonrotating frame that would lead to unusual boundary conditions as the surface terrain moved through the grid) with only two terms that are somewhat nonconventional: gravity and the Coriolis acceleration. Gravity in this frame is directed in the radial direction, which implies that it has components in all three coordinate directions. The Coriolis force is by definition $-2\rho\mathbf{\Omega} \times \mathbf{V}$ and likewise has components in all three directions.

### b. Physical formulations

OMEGA uses a fully elastic nonhydrostatic equation set for the atmospheric part of the system. For brevity, we classify the five mixing ratios for water substances into three groups: water vapor $Q_v$; precipitating water substances $Q_p$ (rain or snow); and nonprecipitating water substances $Q_n$ (ice crystals or water droplets). Furthermore, we cast the equations in their conservative form consistent with the fully elastic mass-conservation equation. This form is better suited for the upwind advection schemes that we used, which have significantly less numerical diffusion (important for the finer resolution we are trying to achieve).

We begin by decomposing the atmospheric pressure and density into a time-invariant hydrostatic base state and a perturbation upon that state such that

$$p(x, y, z, t) = p_0(x, y, z) + p'(x, y, z, t), \quad \text{and} \quad (1)$$

$$\rho(x, y, z, t) = \rho_0(x, y, z) + \rho'(x, y, z, t). \quad (2)$$

We then have the following equation set for the conservation of mass, momentum, and energy:

$$\frac{\partial \rho}{\partial t} + \nabla \cdot (\rho \mathbf{V}) = F_\rho,$$

$$\frac{\partial \rho Q_v}{\partial t} + \nabla \cdot (\rho Q_v \mathbf{V}) = \rho M_v + F_{Q_v},$$

$$\frac{\partial \rho Q_n}{\partial t} + \nabla \cdot (\rho Q_n \mathbf{V}) = \rho M_n + F_{Q_n},$$

$$\frac{\partial \rho Q_p}{\partial t} + \nabla \cdot (\rho Q_p \mathbf{V}) = \rho M_p + \frac{\partial}{\partial z}(Q_p W_p \rho) + F_{Q_p}, \quad \text{and}$$

$$\frac{\partial \rho Q_a}{\partial t} + \nabla \cdot (\rho Q_a \mathbf{V}) = \rho M_a + \frac{\partial}{\partial t}(Q_a W_a \rho) + F_{Q_a}, \quad (3)$$

where the subscript $a$ refers to aerosols or gases. In Eq. (3), $\rho$ represents the dry air density, calculated from the total density $\rho_t$ as

$$\rho = \rho_t/(1 + Q_v). \quad (4)$$

Therefore,

$$\frac{\partial \rho_t \mathbf{V}}{\partial t} + \nabla \cdot (\rho_t \mathbf{V}\mathbf{V}) = -\nabla p' - (\rho_t - \rho_0) g\hat{r} - 2\rho_t \mathbf{\Omega} \times \mathbf{V} + \mathbf{F}_M, \quad \text{and} \quad (5)$$

$$\frac{\partial E}{\partial t} + \nabla \cdot (E\mathbf{V}) = \frac{E}{c_p T} \sum_j (L_j S_j) + S_R + F_h, \quad (6)$$

where $E$ is the energy density.

The terms have been arranged such that the conservative advection terms appear on the left side of each equation. The source terms on the right side of the momentum equation include buoyancy and gravitational effects $-(\rho_t - \rho_0)g\hat{r}$ (where $\hat{r}$ is the radial unit vector) and the Coriolis force ($-2\rho\mathbf{\Omega} \times \mathbf{V}$). Variable $F$ represents the subgrid-scale turbulence contributions. For the remaining equations, $T$ is the temperature, $L_j$ and $S_j$ denote the latent heat and rate of phase conversion of either vaporization, fusion, or sublimation, and $W_p$ represents the terminal velocity of each of the precipitating water substances. Here, $S_j$ depends on the microphysics

that governs the phase transitions and $W_a$ depends on the assumed size distribution and mass of the hydrometeors. Variables $M_n$ and $M_p$ are the nonprecipitating and precipitating microphysics source terms, and $S_R$ is the contribution of radiation flux to heating the atmosphere.

The parameterization of turbulence in OMEGA [i.e., the forcing terms $F$ in Eqs. (3), (5), and (6)] is accomplished using a detailed physical model for the planetary boundary layer (PBL) with a 2.5-level Mellor and Yamada (1974) closure scheme, which is a 1.5-order turbulent kinetic energy closure scheme. In this PBL scheme, the revised formulas proposed by Beljaars and Holtslag (1991) are used for the surface layer. The land surface module implemented in OMEGA is based on the scheme proposed by Noilhan and Planton (1989) and uses worldwide datasets for soil type, land use/land cover, vegetation index, climatological sea surface temperature, climatological subsurface temperature, and climatological soil moisture.

The OMEGA microphysics package falls under the category of bulk-water microphysics in which the production rates are functions of the total mass density of each water species (Lin et al. 1983). Although the goal of OMEGA is to try to explicitly resolve large areas of convection, there will always be regions that are not sufficiently resolved. To circumvent this problem a version of cumulus parameterization that was originally proposed by Kuo (1965, 1974) and later modified by Anthes (1977) is incorporated to account for the effect of subgrid-scale deep cumulus convection on the local environment. The radiative source and/or sink term in the conservation of energy relation [Eq. (6)] is treated as the temperature change resulting from longwave and shortwave radiative divergence flux in the vertical direction (Mahrer and Pielke 1977). The method of parameterizing this vertical flux takes into account the absorption of shortwave radiation by water vapor and the longwave energy emitted by water vapor and carbon dioxide using the computationally efficient technique of Sasamori (1972).

### c. Model initial and boundary conditions

The OMEGA data preprocessor converts a diverse mixture of real-time atmospheric data into initial and boundary conditions for an OMEGA simulation. The OMEGA preprocessor can ingest real-time atmospheric data from the National Centers for Environmental Prediction (NCEP) and the U.S. Navy Fleet Numerical Meteorology and Oceanography Center. The environment outside the computational domain is derived from the same larger-scale forecast models. The lateral boundaries are open and allow the unimpeded flow of air. To allow the propagation of acoustic disturbances across the lateral boundaries, we use a radiative boundary condition with a uniform phase speed. The upper boundary is a rigid, free-slip surface. Last, the surface boundary conditions applied in OMEGA are formulated with the aid of Monin–Obukhov similarity theory.

### d. The Atmospheric Dispersion Model

The Atmospheric Dispersion Model (ADM) is embedded within OMEGA. By embedding the dispersion model, the transport and diffusion algorithms have access to the meteorological data at the OMEGA model spatial and temporal resolution. The potential benefit of embedded transport has been demonstrated in Zannetti (1996). The ADM is composed of a Lagrangian dispersion algorithm that advects tracers using the OMEGA-resolved wind field while simultaneously solving a diffusion model that simulates the effect of unresolved subgrid-scale turbulence. The Lagrangian particle model provides a comprehensive injection and dispersion capability for particles or discrete mass elements. The user can also choose the altitude of release, the injection time interval, the start and stop time of the injection, the number of particles (or puff centroids) to be released, and also whether to initialize multiple release locations for the particles.

The Lagrangian particle model simulates the dispersion of pollutants in the atmosphere by means of a large ensemble of Lagrangian particles moving at each time step with pseudovelocities. These pseudovelocities simulate the effects of the two basic dispersion components: 1) transport due to the mean wind, and 2) diffusion due to turbulent velocity fluctuations. Subsequent positions of each particle ($x$, $y$, $z$) representing a discrete element of pollutant mass are computed from the following:

$$x(t + \Delta t) = x(t) + [\overline{u}(t) + u'(t)]\Delta t, \quad (7)$$

$$y(t + \Delta t) = y(t) + [\overline{v}(t) + v'(t)]\Delta t, \quad \text{and} \quad (8)$$

$$z(t + \Delta t) = z(t) + [\overline{w}(t) + w'(t)]\Delta t, \quad (9)$$

where $\overline{u}$, $\overline{v}$, and $\overline{w}$ are the OMEGA-predicted mean wind components, and $u'$, $v'$, and $w'$ are the corresponding subgrid-scale turbulent velocity fluctuations in each of the three directions.

The subgrid-scale turbulent velocity fluctuations are derived from a first-order Markov process defined by

$$u'(t) = R_u(\Delta t)u'(t - \Delta t) + [1 - R_u^2(\Delta t)]^{1/2}\sigma_u r_u, \quad (10)$$

$$v'(t) = R_v(\Delta t)v'(t - \Delta t) + [1 - R_v^2(\Delta t)]^{1/2}\sigma_v r_v, \quad (11)$$

and

$$w'(t) = R_w(\Delta t)w'(t - \Delta t) + [1 - R_w^2(\Delta t)]^{1/2}\sigma_w r_w + [1 - R_w(\Delta t)]T_{Lw}\frac{\partial \sigma_w^2}{\partial z}, \quad (12)$$

where $R_u$, $R_v$, and $R_w$ are autocorrelation coefficients for lag time $\Delta t$ and are assumed to be exponential and $r_u$, $r_v$, and $r_w$ are random numbers with zero mean and unit standard deviation (e.g., see Yamada and Bunker 1988; Uliasz 1990; Boybeyi et al. 1995). The Lagrang-

ian turbulent statistics such as the standard deviations of velocity components ($\sigma_u$, $\sigma_v$, $\sigma_w$) and Lagrangian integral timescales ($T_L^u$, $T_L^v$, $T_L^w$) are calculated similar to Uliasz (1990).

A ''kernel'' density estimator is then used to calculate concentration values. Since each particle represents a center of a puff, various functional forms may be assumed to express the concentration distribution in the puff. One of the simplest ways is to assume a Gaussian distribution where the spatial extent grows with time (Lorimer 1986; Yamada and Bunker 1988). The concentration level at a given time and space (at a receptor location) is determined as the sum of the concentrations each puff contributes:

$$C(x, y, z) = \frac{m_p}{(2\pi)^{3/2}} \sum_{k=1}^{N} \frac{1}{\sigma_{xk}\sigma_{yk}\sigma_{zk}} \left\{ \exp\left[ -\frac{(X_k - x)^2}{2\sigma_{xk}^2} \right] \right\} \times \left\{ \exp\left[ -\frac{(Y_k - y)^2}{2\sigma_{yk}^2} \right] \right\} \times \left\{ \exp\left[ -\frac{(Z_k - z)^2}{2\sigma_{zk}^2} \right] + \exp\left[ -\frac{(Z_k + z)^2}{2\sigma_{zk}^2} \right] \right\}, \quad (13)$$

where $X_k$, $Y_k$, and $Z_k$ are center coordinates of the $k$th puff. The spatial extents of the Gaussian distribution $\sigma_{xk}$, $\sigma_{yk}$, and $\sigma_{zk}$ are estimated based on Taylor's homogeneous diffusion theory (Taylor 1921; Uliasz 1990; Yamada and Bunker 1988).

## 3. An overview of ETEX

Observations of mesoscale atmospheric dispersion formed the foundation of most of our current understanding of this phenomenon and provided the impetus for many theoretical and numerical studies. However, relatively few mesoscale atmospheric dispersion observations exist as compared with the large number of observations of short-range dispersion experiments [e.g., Solent experiment in Emberlin (1981); Oxnard Plain experiment in Lamb et al. (1978); Atmospheric Studies in Complex Terrain '84 in Clements et al. (1989)]. The majority of the mesoscale experiments have been carried out in the last two decades, reflecting both the recent development of suitable tracers and analysis techniques and a heightened interest of various research groups and funding agencies in mesoscale atmospheric dispersion. Among the major mesoscale atmospheric dispersion experiments are the Great Plains Experiment (Ferber et al. 1981), the Atlantic Coast Unique Regional Atmospheric Tracer Experiment (Heffter et al. 1984), the Cross-Appalachian Tracer Experiment (Ferber et al. 1986), and the Across North America Tracer Experiment (Draxler and Heffter 1989).

A significant mesoscale atmospheric dispersion exercise in recent years was the European Tracer Experiment (Nodop et al. 1998; van Dop et al. 1998; Graziani et al. 1998). A cloud of an inert tracer (a perfluorocarbon) was released from a point source located in northwestern France. The participants in the exercise were informed of the exact time, location, release characteristics, and other local data only after it occurred. The forecast of the plume evolution for 60 h over the width of Europe was reported by each participant as soon as possible thereafter, utilizing the meteorological information available to them. The participants updated their forecast in real time as new meteorological information became available to them over the 60-h period. The forecast of surface concentrations was subsequently compared with measured concentrations at 168 ground-level sampling locations across Europe. The ETEX experiment contained two separate tracer release periods. The first period took place on 23–26 October 1994 (Girardi et al. 1997). The exercise was repeated approximately one month later on 13–16 November 1994 for a second tracer release. In this study, the first ETEX release period is simulated by OMEGA.

### *a. Meteorological situation during the first release*

A preliminary meteorological statistical study revealed that the most suitable weather situation for a successful experiment (i.e., the highest number of ground sampling stations and the majority of European countries hit by the tracer plume), relatively easy to forecast and most likely to occur, was one with westerly flows over central Europe. Figure 2 shows the surface pressure maps for the European continent on 23–26 October 1994 as analyzed by ECMWF. Prior to the beginning of the time window for the experiment, a high pressure cell extended over central Europe, thereby causing an easterly to southeasterly flow in this area. During that period, there was also an upper-air ridge of high pressure, blocking the approach of oceanic frontal systems. With an easterly movement of the high pressure system, a cold front finally passed the release site on the morning of Saturday, 22 October. After this frontal passage, a period with rather strong westerly winds was advecting an unstable air mass over Europe.

The synoptic situation on 0000 UTC 23 October showed that a deep low pressure system (with a central pressure value of about 975 mb) was located east of Scotland. This low pressure system was slowly moving northward and maintaining a strong southwesterly flow over most of Europe. The cold front associated with this low pressure system was also progressing toward east, advecting unstable air with showers, and some were accompanied by thunder and squall lines east of the release site. By 0000 UTC 24 October, France and western Europe remained in a westerly perturbed flow. There was still an unstable flow over the area of interest. The wind in the area of interest was decreasing because of the northerly movement of the surface low over the North Sea. The cold front was moving eastward, car-

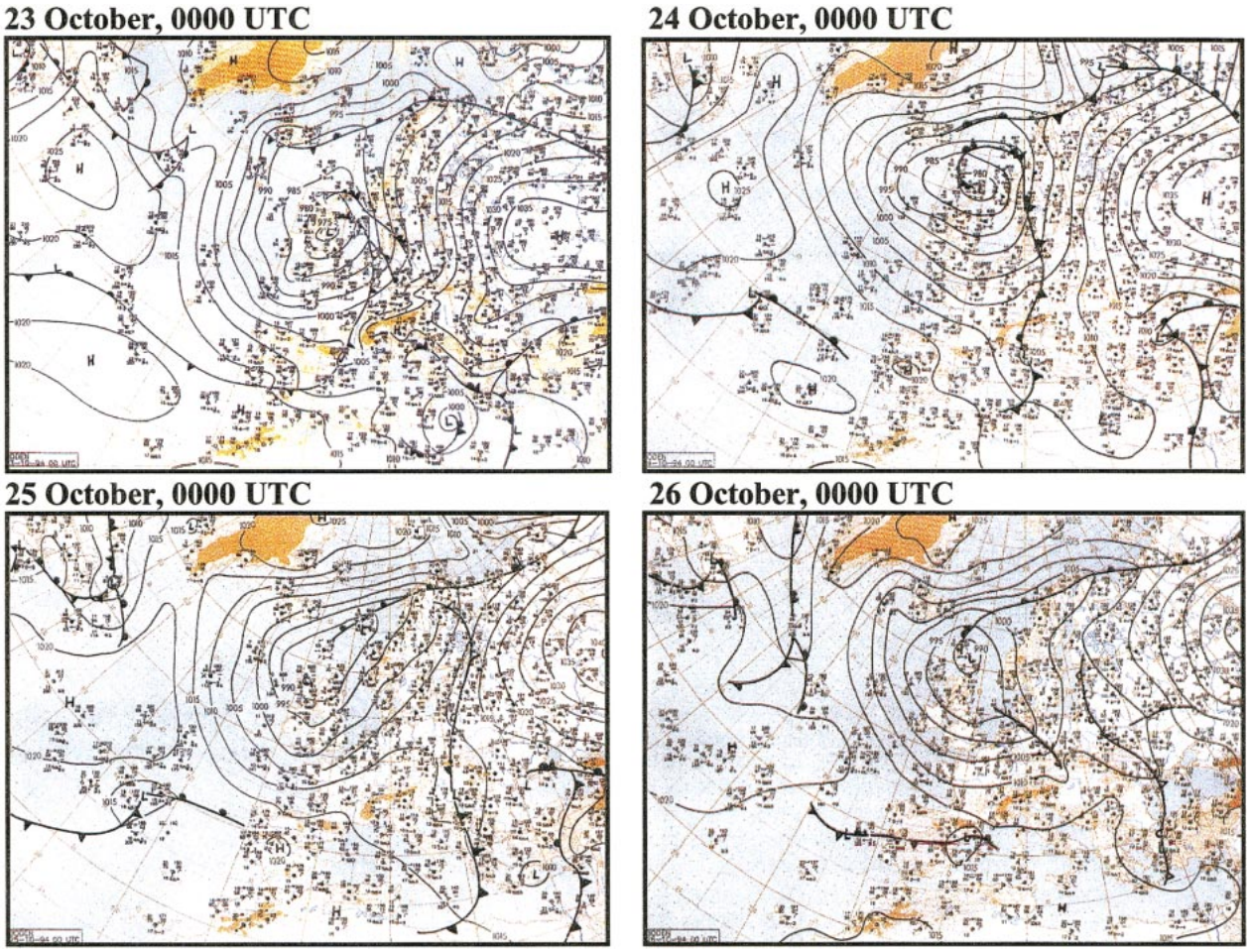


FIG. 2. The synoptic situation during the first ETEX release period of 23–26 Oct 1994 over the European continent as analyzed by the ECMWF (from Graziani et al. 1998).

rying showers to Germany with weakened instability. By 0000 UTC 25 October, the cold front moved farther eastward. Weak convection was still developing along the cold front, giving rise to thunderstorms and showers over eastern Europe. By 0000 UTC 26 October, the deep low pressure system was still located over the North Sea and Scotland (with a central pressure value of about 990 mb), and hence still maintaining the strong southwesterly flow over Europe.

The above meteorological conditions indicated that the weather during the release was characterized by a rather strong west to southwesterly flow, which could advect the tracer in the correct direction (i.e., the majority of European countries hit by the tracer plume). No frontal system was foreseen to pass over the release site shortly before, during, or after the release. During the exercise days (23–26 October 1994), the general circulation over Europe was very slowly changing. Therefore, the overall weather conditions were very suitable for a successful experiment.

TABLE 2. Release characteristics of the first ETEX exercise.

| | |
|---|---|
| Release location | Monterfil (48°03′30″N, 2°00′30″W) |
| Release height | 8 m above ground level |
| Release start time | 1600 UTC 23 Oct 1994 |
| Release duration | 12 h |
| Tracer | Perfluoro-methyl-cyclo-hexane |
| Tracer properties | Inert, nondepositing, nonwater-soluble |
| Quantity of PMCH released | 340 kg |
| Source strength | 7.95 g $s^{-1}$ |
| Exit temperature | 84°C |
| Exit velocity | 45 m $s^{-1}$ |

### *b. Source, sampling network, and data during the first ETEX release period*

The first ETEX exercise took place on 23 October 1994, and its release characteristics are summarized in Table 2. The release site was located approximately 35 km west of Rennes, at Monterfil, in Brittany, France,

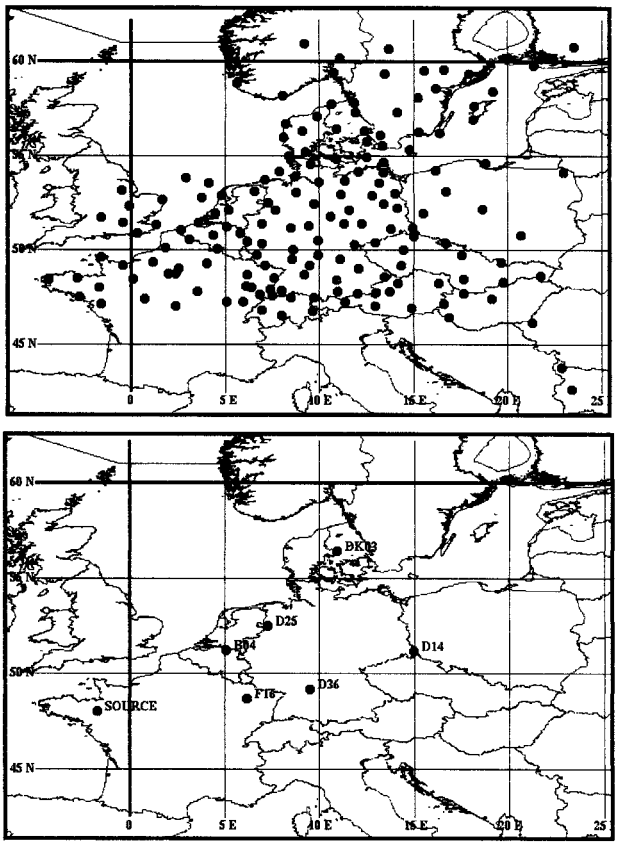


FIG. 3. (top) Locations of the 168 concentration-sampling stations, and (bottom) the release site labeled ''SOURCE'' and six sampling stations selected for the time analysis later in this section.

90 m above sea level (Fig. 3). The tracer was perfluoromethyl-cyclo-hexane (PMCH), which is a suitable tracer substance for experiments over long distances. PMCH is a nontoxic, nondepositing, nonwater-soluble, inert and environmentally safe tracer. The tracer release started on 1600 UTC 23 October and ended on 0350 UTC 24 October. During these nearly 12 h, a total of 340 kg of PMCH was emitted into the atmosphere resulting in an average release rate of 7.95 g $s^{-1}$. The airstream (67 $m^3$ $h^{-1}$) at the top of the release chimney (8 m above ground) had an average temperature of 84°C and a velocity of about 45 m $s^{-1}$. The mass released and the release rate were chosen so that the expected concentration values, even at the most distant sampler, would be high enough relative to normal background levels to ensure successful chemical analysis. At the same time, these rates were low enough to maintain global background levels as low as possible and to minimize the cost of the release.

The ground-level sampling locations consisted of 168 sites throughout Europe east of the release site (Fig. 3). At these sites, automated sequential air samplers sampled air every 3 h for a total of 72 h. The stations closer to the source started sampling 3 h before the release started, and the most distant stations delayed the start of sampling such that they only finished 90 h after the release start. Background values were measured before, during, and after the experiment at many stations. Average background was then subtracted from the measured values at all the stations. The measurements indicated that a level of 0.01 ng $m^{-3}$ could be used as lower limit in the statistical comparison with model results.

The evolution of the measured surface concentration at 24, 36, 48, and 60 h after the start of the release, as determined by the ETEX organizers (Graziani et al. 1998), is presented in Fig. 4. The reconstruction of the cloud positions and shapes from the measurements revealed that even the relatively uncomplicated meteorological conditions of westerly winds (frequently occuring in Europe) produced an unexpected cloud behavior at 24 h. After 24 h, the tracer cloud, as derived from a spatial interpolation of the measured data, moved in a easterly to northeasterly direction and split into two parts. The splitting may be due to a real effect (hence the lack of observation at one critical station) or due to some observation error. To date, the cause of splitting has not been well understood. The cloud center traveled substantially and was close to the border between Belgium and Germany; some Dutch territory was also involved. After 36 h, the cloud position confirmed that the tracer mostly left France. The peak was now in Germany and there were no indications of any splitting of the tracer cloud into two or more parts, with the exception of a nonzero measurement in Romania.

Later (after 48 h), the cloud position elongated from the previous W–E direction to the S–N direction covering a wide area over various countries (Germany, Denmark, Czech Republic, Slovak Republic, Hungary, Romania, and Poland). By this hour, sites in Norway and Sweden also started to detect the tracer arrival. Finally, after 60 h, the cloud elongation continued stretching the tracer cloud over the North Sea between Denmark and Norway. By this hour, the higher contour lines show the presence of two peak regions.

Overall, the surface concentration measurements indicated that the measured concentration values of tracer were well above 1.5 ng $m^{-3}$ at many stations close to the release site. The highest concentration value was measured as 12.75 ng $m^{-3}$ at Rennes, 30 km away from the release site. As the tracer cloud moved to central Europe later in time, tracer concentration values ranging from 0.12 to 0.75 ng $m^{-3}$ were detected, and these values lasted for a long period of time. Farther downwind, in Bulgaria, more than 2000 km away from the release site, the measured concentration values were about 0.03 ng $m^{-3}$ above the background value.

## 4. OMEGA model parameters

The OMEGA model for this case was run for a 72-h forecast period starting on 1200 UTC 23 October. The tracer release started on 1600 UTC 23 October and con-

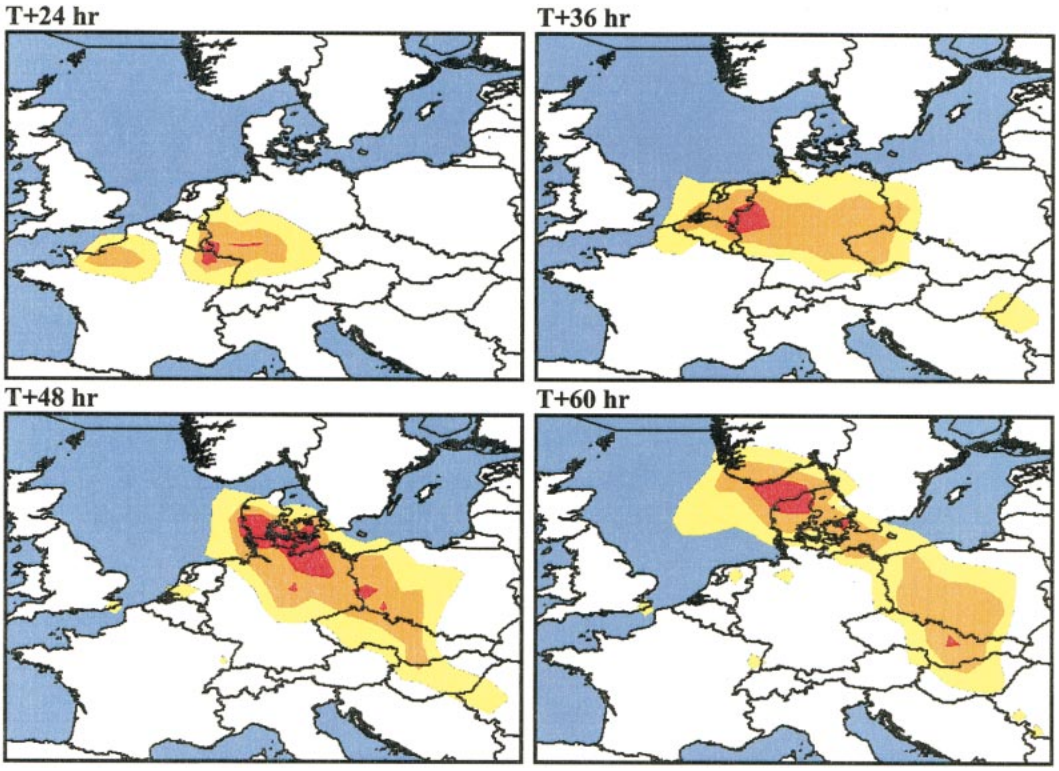


FIG. 4. Contours of 3-h average air concentration measured at sampling sites for periods ending at 24, 36, 48, and 60 h after the start of the release (respectively, 1200–1500 UTC 25 Oct; 0000–0300 UTC 25 Oct; 1200–1500 UTC 25 Oct; and 0000–0300 UTC 26 Oct). Contour levels are 0.01 (yellow), 0.10 (orange), and 0.50 (red) ng $m^{-3}$ (from Graziani et al. 1998).

tinued for 12 h. It was assumed that the tracer was neutrally buoyant. The computational domain and the static grid configuration (the grid does not change during the integration) used in the simulation are shown in Fig. 5. The simulation domain covered most of the European continent. A horizontal grid resolution ranging from 40 to 100 km was used in the simulation with about 4000 grid cells. The OMEGA model used 31 vertical grid levels for the simulation, with a vertical resolution ranging from 15 m near the ground to 1 km at the top of the domain. The top of the simulation domain was set to 15 km.

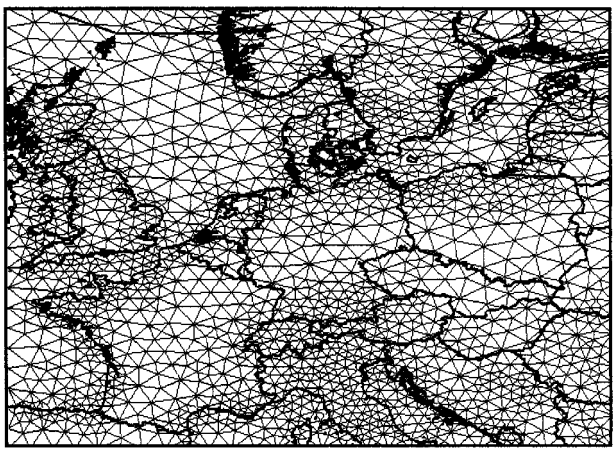

FIG. 5. OMEGA simulation domain and grid configuration. Note that the OMEGA grid was statically adapted to underlying terrain features (not shown in this figure) and land–water boundaries.

The OMEGA model was initialized using Medium-Range Forecast model (MRF) gridded data from NCEP. The conventional surface observational data and rawinsonde observational data were used to complete the analysis of the initial conditions. The environment outside the computational domains was also derived from the same gridded forecast data fields (not from MRF analysis fields). Boundary conditions at 12-h intervals were based on these large-scale gridded forecast fields, and linear interpolation was used to determine boundary values at intermediate times.

An important feature of the OMEGA model is its worldwide datasets. The OMEGA model has eight major worldwide databases for terrain elevation, land/water distribution, soil type, land use/land cover, climatological vegetation index, climatological sea surface temperature, climatological subsurface temperature, and climatological soil moisture. In this simulation, OMEGA used its global terrain elevation and land/water datasets at 5-arc min (10 km) and 30-arc s (1 km). The other

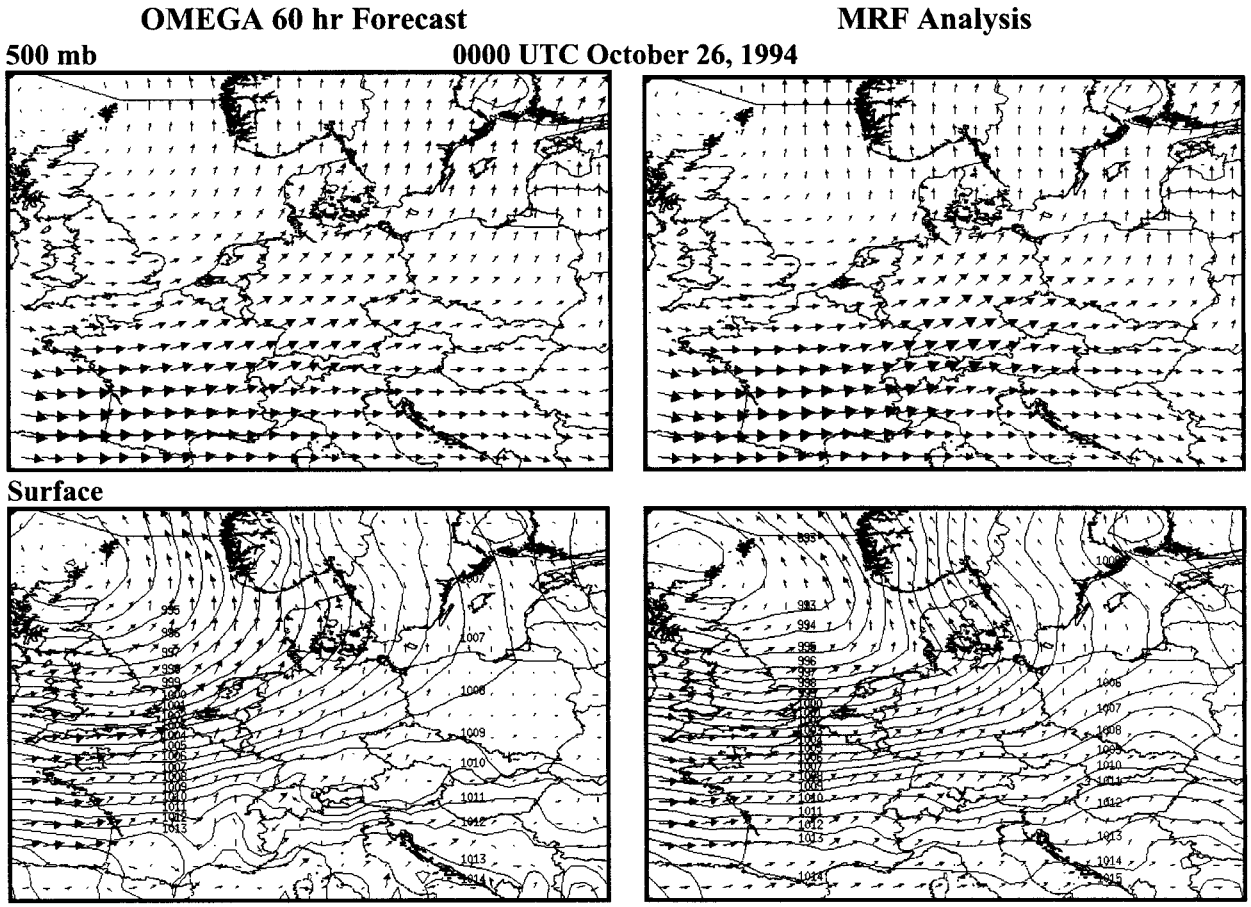


FIG. 6. (left) OMEGA-predicted and (right) MRF-analysis (top) 500-mb and (bottom) surface flow field (vectors are scaled such that the reference wind vector is equal to 20 m $s^{-1}$ at 500 mb and 10 m $s^{-1}$ for the surface level). In addition, the mean sea level pressure (presented at 1-mb interval) at 0000 UTC 26 Oct 1994 and the corresponding MRF analysis are shown. Note that the OMEGA-predicted wind vectors are interpolated on a regularly spaced grid for clarity of the figure.

characteristics were obtained from different sources. For example, a 1° global soil-type database (12 types), created from the Global Ecosystems Database (Webb et al. 1992), was used in this simulation. Similarly, 19 land-cover categories from the Biosphere–Atmosphere Transfer Scheme with a 30-arc s (1 km) resolution were used for land use/land cover data. Last, sea surface temperature, ground temperature, and soil moisture information were specified from the initial conditions.

## 5. Discussion of results

In this section, we will evaluate the OMEGA-predicted meteorological and dispersion fields against meteorological and dispersion observations both qualitatively and quantitatively. The following section will discuss the comparisons between the predicted and observed nature of the state of the atmosphere and associated dispersion characteristics.

### *a. Meteorological behavior*

In order to understand the dispersion of atmospheric pollutants over mesoscale travel times and distances, it is first necessary to understand the behavior of atmospheric flows on these scales. We start with the synoptic dynamical processes, associated with the 3-day period of the first ETEX release. The synoptic-scale analysis began with an examination of the standard 500-mb and near-surface flow fields. Figure 6 depicts the OMEGA-predicted flow field superimposed on the mean sea level pressure field and the corresponding MRF analysis fields interpolated on the OMEGA grid for the 500-mb and near-surface levels at 0000 UTC 26 October 1994 (60 h into the forecast). Because the large-scale synoptic pattern did not change considerably during the experimental period, only the 60-h comparison will be discussed here for brevity. For clarity, the OMEGA-predicted wind vectors shown in Fig. 6 have been interpolated onto a regularly spaced grid.

The MRF analyses (Fig. 6, right panels) indicate that

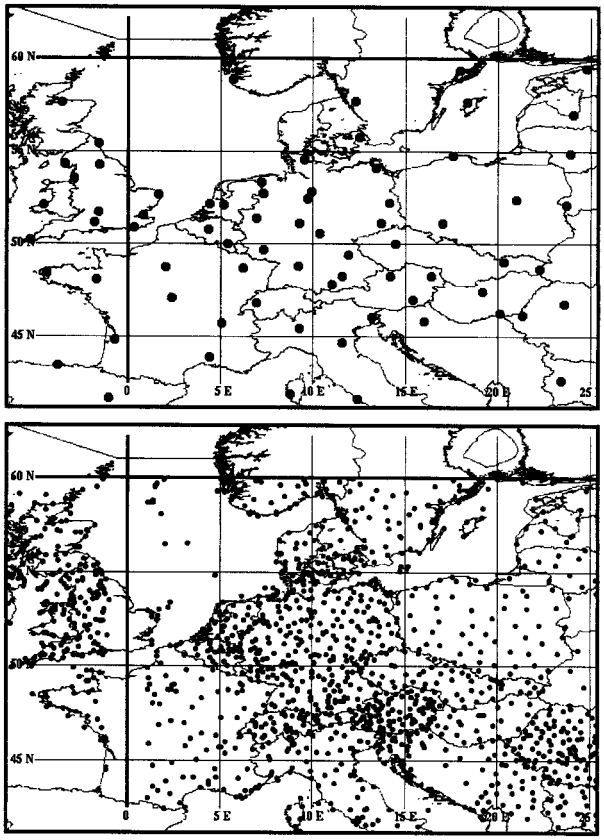


FIG. 7. The locations of the (top) roughly 75 rawinsonde and (bottom) roughly 1200 surface observational sites.

the weather during the experiment was dominated by a deep low pressure system centered north of Scotland. This prevailing large-scale synoptic pattern was nearly steady and driving a southwesterly flow over most of Europe during the period of the tracer experiment. This low pressure system and the cold front associated with it progressed very slowly northward during the simulation and set a complex cyclonic circulation over the North Sea and Scotland. This cyclonic circulation had a central pressure of about 991 mb (bottom right) by this time.

The OMEGA model predicted the location and strength of the cyclonic circulation with a reasonable accuracy as compared with the data analysis. The OMEGA model had the low with a central pressure of about 992 mb, with the 1-mb discrepancy possibly due to differences in sea level pressure reduction. Another discrepancy between the simulation results and the observations was that the OMEGA results show stronger terrain features, particularly near the surface. Although the large-scale synoptic pattern did not change considerably during the experimental period, ETEX was still an inherently complex case because of its large domain with complicated topography and long sampling period. As a result, flow perturbations induced by terrain-forced mesoscale circulations perhaps played a significant role in the dispersion of the tracer cloud.

During the experiment, meteorological information on the state of the atmosphere was also collected, vital for the comparison of the measurements and modeled fields. The meteorological database contains both surface and rawinsonde observations collected from the time of the tracer release and 3 days ahead. The locations of surface observational (about 1200 locations) and rawinsonde observational sites (75 locations) are displayed in Fig. 7. The data collected from all these sites were first used to complete the analysis of the initial conditions and then were used to compare quantitatively with the corresponding OMEGA predicted fields.

#### 1) SURFACE OBSERVATION COMPARISON

To compare surface observational data with the output of OMEGA, a postprocessor was developed that locates the observational points on the OMEGA grid and outputs OMEGA-predicted fields at the closest OMEGA grid point to these locations. These fields were then compared with the actual observations, and the error statistics were calculated without performing data quality control on the observations. In other words, the surface observations were used as they were reported. The statistics produced were mean error, mean-absolute error, and root-mean-square error, which are defined as follows:

$$\text{Mean Error (ME)} = \frac{1}{N}\sum (f_P - f_O),$$

$$\text{Mean-Absolute Error (MAE)} = \frac{1}{N}\sum |(f_P - f_O)|,$$

and

$$\text{Root-Mean-Square Error (rmse)} = \sqrt{\frac{1}{N}\sum (f_P - f_O)^2}, \tag{14}$$

where $N$ is the total number of observations, $f$ is the meteorological variable (temperature, wind speed, or wind direction) on which the statistics are calculated, and the suffixes $P$ and $O$ refer to its predicted and observed values, respectively. The ME provides a measure of the bias in the prediction of the variable; the MAE measures the average deviation of the prediction from the observations; and rmse estimates a kind of generalized standard deviation.

Table 3 shows the calculated error statistics for surface air temperature, wind speed, and wind direction. The error statistics were generated at the initial time (0 h) and at 24-, 48-, and 72-h forecast times for comparison of errors in initial fields against errors in forecast fields. For example, surface temperature statistics generally indicate less than 0.5-K temperature bias, less than 2.5-K MAE, and less than 3.0-K rmse. Surface

TABLE 3. Surface error statistics. Note that 0 h is the OMEGA model initial field, and 24, 48, 72 h are the OMEGA model forecast fields. (About 1200 surface stations presented in Fig. 7 are processed to generate each of these statistics.)

| Parameter | Forecast time (h) | No. of obs | ME | MAE | Rmse |
|---|---|---|---|---|---|
| Temperature (K) | 0 | 1151 | −0.01 | 2.33 | 3.05 |
| | 24 | 1234 | −0.24 | 2.13 | 2.86 |
| | 48 | 1233 | −0.30 | 2.17 | 2.88 |
| | 72 | 1240 | 0.28 | 2.11 | 2.73 |
| Wind speed (m s$^{-1}$) | 0 | 1061 | 0.26 | 2.34 | 2.98 |
| | 24 | 1140 | −0.34 | 1.67 | 2.23 |
| | 48 | 1136 | −0.47 | 1.87 | 2.48 |
| | 72 | 1162 | −0.57 | 1.92 | 2.54 |
| Wind direction (°) | 0 | 1061 | −11.72 | 35.02 | 49.19 |
| | 24 | 1140 | 1.82 | 32.78 | 47.60 |
| | 48 | 1136 | 3.76 | 34.81 | 46.94 |
| | 72 | 1162 | 4.27 | 31.80 | 44.92 |

wind speed shows less than 0.5 m s$^{-1}$ bias, less than 2 m s$^{-1}$ MAE, and less than 3 m s$^{-1}$ rmse. Surface wind direction shows less than 5° bias, about 35° MAE, and about 45° rmse. One important feature of these statistical results is that the OMEGA model forecast shows relatively stable behavior with a small degradation during the simulation at all times. In fact, many of the errors come from the initial field. For example, MAE and rmse for all three variables (temperature, wind speed, and wind direction) are about the same as forecast errors.

The surface forecast error statistics may also be attributed to several other factors. First, the inclusion of all surface data in the statistics, even data that were rejected by the quality control system during the analysis, leads to a higher rmse than would have occurred if only data accepted by the quality control system were used. Second, there will be differences between the actual observation height and the computed height. For example, the OMEGA model used the lower-cell parameters without correction. This effective parameter height is 15 m for scalars and 30 m for momentum. Third, the differences may be due to the subgrid variability present in the real-world. The observed data were affected by local structures and terrain features; with a horizontal grid resolution in excess of 40 km, these local features could not be modeled accurately.

### 2) RAWINSONDE OBSERVATION COMPARISON

The rawinsonde observations were also compared with the output of OMEGA. Over 500 soundings were processed to generate statistics for ME, MAE, and rmse as a function of forecast time and altitude level. Table 4 presents the results of this analysis where all levels below the indicated level are accumulated to produce the reported statistic. This table shows that there is a noticeable growth in the temperature and wind direction biases over 72 h and some growth in the rmse for temperature, but that the other values stay relatively constant. A somewhat different analysis demonstrated that 88% of the predicted upper-air temperatures are within 2.5 K of the observed value and 99% are within 5.0 K. The same analysis indicated that the predicted upper-air wind speed is within 2.5 m s$^{-1}$ of the observed value 50% of the time and within 5 m s$^{-1}$ 81% of the time, and the predicted upper-air wind direction is within 15°

TABLE 4. Upper-air error statistics. Note that 0 h is the OMEGA model initial field, and 24, 48, 72 h are the OMEGA model forecast fields. (About 75 rawinsonde stations presented in Fig. 7 are processed to generate each of these statistics.)

Temperature

| Pressure level | Average No. points | ME (K) | | | | Rmse (K) | | | |
|---|---|---|---|---|---|---|---|---|---|
| | | 0 h | 24 h | 48 h | 72 h | 0 h | 24 h | 48 h | 72 h |
| <100 mb | 573 | 0.00 | 0.58 | 0.70 | 1.44 | 1.38 | 1.52 | 1.65 | 2.43 |
| <350 mb | 499 | −0.03 | 0.50 | 0.51 | 1.27 | 1.40 | 1.50 | 1.51 | 2.22 |
| <500 mb | 391 | −0.02 | 0.29 | 0.40 | 0.88 | 1.51 | 1.34 | 1.49 | 1.73 |
| <850 mb | 123 | 0.00 | 0.12 | 0.30 | 0.65 | 2.27 | 1.52 | 1.81 | 2.10 |

Wind speed

| Pressure level | Average No. points | ME (m s$^{-1}$) | | | | Rmse (m s$^{-1}$) | | | |
|---|---|---|---|---|---|---|---|---|---|
| | | 0 h | 24 h | 48 h | 72 h | 0 h | 24 h | 48 h | 72 h |
| <100 mb | 344 | −1.33 | −0.61 | −1.26 | −1.64 | 4.67 | 4.96 | 4.51 | 5.79 |
| <350 mb | 289 | −1.12 | −0.02 | −1.00 | −1.47 | 4.33 | 3.37 | 3.96 | 5.02 |
| <500 mb | 228 | −1.01 | 0.10 | −0.84 | −1.55 | 4.14 | 2.71 | 3.48 | 4.02 |
| <850 mb | 94 | −1.24 | 0.12 | −0.70 | −1.17 | 3.68 | 2.43 | 3.34 | 3.10 |

Wind direction

| Pressure level | Average No. points | ME (°) | | | | Rmse (°) | | | |
|---|---|---|---|---|---|---|---|---|---|
| | | 0 h | 24 h | 48 h | 72 h | 0 h | 24 h | 48 h | 72 h |
| <100 mb | 344 | −1.40 | 4.99 | 5.47 | 8.02 | 28.11 | 27.14 | 27.61 | 28.02 |
| <350 mb | 289 | −2.04 | 6.39 | 5.43 | 9.42 | 29.73 | 27.01 | 28.50 | 29.83 |
| <500 mb | 228 | −2.58 | 6.86 | 6.28 | 10.01 | 32.69 | 28.01 | 29.52 | 32.62 |
| <850 mb | 94 | −2.40 | 12.89 | 12.66 | 15.42 | 46.39 | 35.55 | 37.19 | 41.36 |

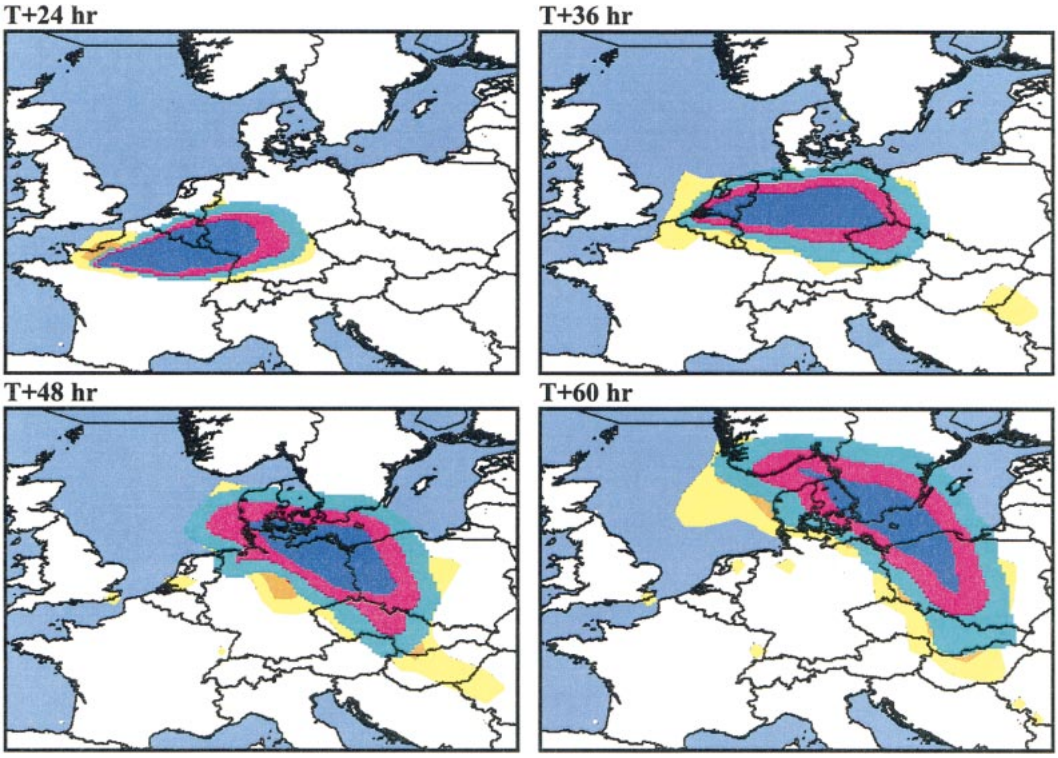


FIG. 8. Contours of 3-h average predicted surface concentration superimposed on the contours of measured concentration presented in Fig. 4 for periods ending at 24, 36, 48, and 60 h after the start of the release. The predicted contour levels are 0.01 (cyan), 0.10 (magenta), and 0.50 (blue) ng $m^{-3}$.

and 30° of the observed value 60% and 84% of the time, respectively. In all of these analyses, the input data were used as is, without performing any quality control to remove easily identifiable bad data; this results in a floor on the rmse.

Overall, the above meteorological results indicated that the OMEGA model predicted the meteorological conditions during the first ETEX exercise reasonably well for 72 h. Since the embedded ADM uses the OMEGA-predicted meteorological fields (such as mean wind components and atmospheric turbulence information) at the OMEGA model's spatial and temporal resolution, the ADM model predicted dispersion characteristics of the tracer cloud will be determined by the OMEGA-predicted meteorological fields.

### *b. Dispersion*

In this section, the predicted dispersion characteristics from the ADM model are compared with the ETEX measurements. Figure 8 presents the predicted 3-h average concentration contours superimposed on the measured 3-h average concentration contours (obtained from Fig. 4) at 24, 36, 48, and 60 h after the start of the release. The contour levels (isolines) presented in the figure are 0.01, 0.1, and 0.50 ng $m^{-3}$. It is important to note that the measured concentration contours in Fig. 8 were produced using measured data from the sampling sites, whereas the concentration contours superimposed were produced using model-calculated data on the model receptor locations. Therefore, the contours shown may not be representative of the concentration pattern in regions poorly sampled by the sampling-site network shown in Fig. 3. Perhaps, this is at least partially responsible for the gap in the measured contours over France (Fig. 4). It can be seen from Fig. 8 that the OMEGA results tracked the ETEX release well even after traveling about 2000 km downwind distance. Differences, however, in duration time and concentration values, particularly 48 h after the start of the release, can be seen from Fig. 8. For example, the model generally overpredicts the concentration maxima areas (cf., 0.50 ng $m^{-3}$ contour level in Figs. 4 and 8). The model-predicted tracer cloud is also faster than the measured tracer cloud especially 60 h after the start of the release.

One interesting aspect of this simulation is the change in low-level transport direction after 48 h. At 24 h, the tracer cloud is predicted in France and over German sites. Note that the tracer release ended on 0400 UTC 24 October so that the leading edge of the tracer cloud is now located over Germany while the trailing edge of the tracer cloud is located in France. At 36 h, the cloud position indicates that the trailing edge of the tracer cloud has mainly left the French territory. The peak is now in Germany. At 48 h, the tracer cloud covers a

broader area over various countries. By this time, cloud position rotates from the previous W–E direction to the S–N direction because of the convergence line in the low-level wind field at the border between Germany and Poland. Speed and directional wind shear clearly cause alongwind elongation of the tracer cloud. At 60 h, the cloud elongation continued farther, and its predicted centerline lies east of the measured cloud centerline.

Measured and OMEGA-predicted 3-h average tracer concentrations were also used in statistical analyses to evaluate the performance of OMEGA. Three types of analyses were generated: global analysis, space analysis, and time analysis. Global analysis considers all the concentration values at any time and location. For this analysis the distribution of the values is important as well as the overall tendency to underestimate or overestimate the measured values, with a quantification of the absolute deviation. Space analysis considers the concentrations at a fixed time all over the domain. This analysis is useful to detect space shifting between predictions and calculations. Time analysis considers the concentrations at a fixed location for the duration of the episode. This analysis can give insight on discrepancies between measured values and calculations that may arise from time shifting. When dealing with measured and calculated values, an important issue however, is the measured concentration values. The same filtering technique used during ETEX is also applied in this study for global, space, and time analysis in the case of measured concentration equal to zero. The measured and predicted pairs ($M_i$, $P_i$) considered are those showing a nonzero measured concentration $M_i$ or having a zero value of $M_i$ but occurring in each station not earlier than two time intervals (6 h) before the arrival of the cloud and not later than two time intervals after the departure of the cloud. Also all the pairs with either lost measurement or missing prediction are excluded from the statistical analysis.

### 1) SPACE ANALYSIS

In order to examine further the similarities and differences between the predicted and measured ground-level concentration contours, the figure of merit in space (FMS) is calculated at a fixed time for a fixed concentration level (0.10 and 0.01 ng m$^{-3}$). The FMS is an effective space analysis index for describing the model performance over the simulation domain at a fixed time (Mosca et al. 1998a,b). It quantifies the fraction of the measured and predicted concentration contour areas that overlap. In other words, the FMS can be seen as a statistical coefficient of the space analysis. The FMS is defined as the ratio between the intersection of the measured ($A_M$) and predicted ($A_P$) areas above a significant concentration level and their union:

$$\text{FMS} = \frac{A_M \cap A_P}{A_M \cup A_P}. \tag{15}$$

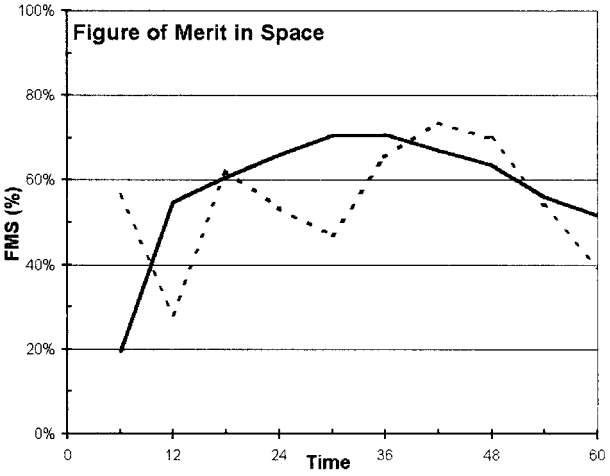


FIG. 9. FMS analysis for 0.01 (solid) and 0.10 (dotted) ng m$^{-3}$ concentration levels.

Thus, the more the model and the measured clouds overlap, the greater the FMS values are. In other words, a high value of the FMS corresponds to good model performance, and a low value of the FMS corresponds to poor model performance.

Figure 9 shows the FMS analysis every 6 h for a total of 60 h after the start of the release for 0.10 ng m$^{-3}$ (middle contour level in Figs. 4 and 8) and 0.01 ng m$^{-3}$ (outer contour level in Figs. 4 and 8) concentration levels. The FMS values for the 0.10 ng m$^{-3}$ concentration level ranges from about 30% to 75% with an average value of 55%, while the FMS values for 0.01 ng m$^3$ concentration levels ranges from 50% to 70% (after a 6-h value of 20%) with an average value of 58%. The variability in the FMS for the 0.10 ng m$^{-3}$ level is due primarily to differences in the predicted area. After the first 12 h, the area of the 0.01 ng m$^{-3}$ contour is within 20% of the measured value; the area of the 0.10 ng m$^{-3}$ contour, however, is greatly affected by the splitting of the cloud (cf. Fig. 4). Later, the FMS values for both the concentration levels show better values.

### 2) GLOBAL ANALYSIS

Quantitative global analysis is also important for evaluating the congruence between the measured and predicted cloud characteristics. The global analysis consists of several scatter diagrams and statistical indices for the measured and the predicted concentration pairs. Scatter diagrams are produced for all concentration pairs, peak concentration pairs, time of arrival, time of peak concentration, and duration time of the cloud. Global statistical indices are produced for the percentage of the predicted values with a factor of 2 (FA2) and 5 (FA5) of the measured values; factor of exceedance (FOEX), an indicator of under- or overestimation; bias, as an indicator of under- or overestimation; normalized mean square error (NMSE) as an indicator of deviation of

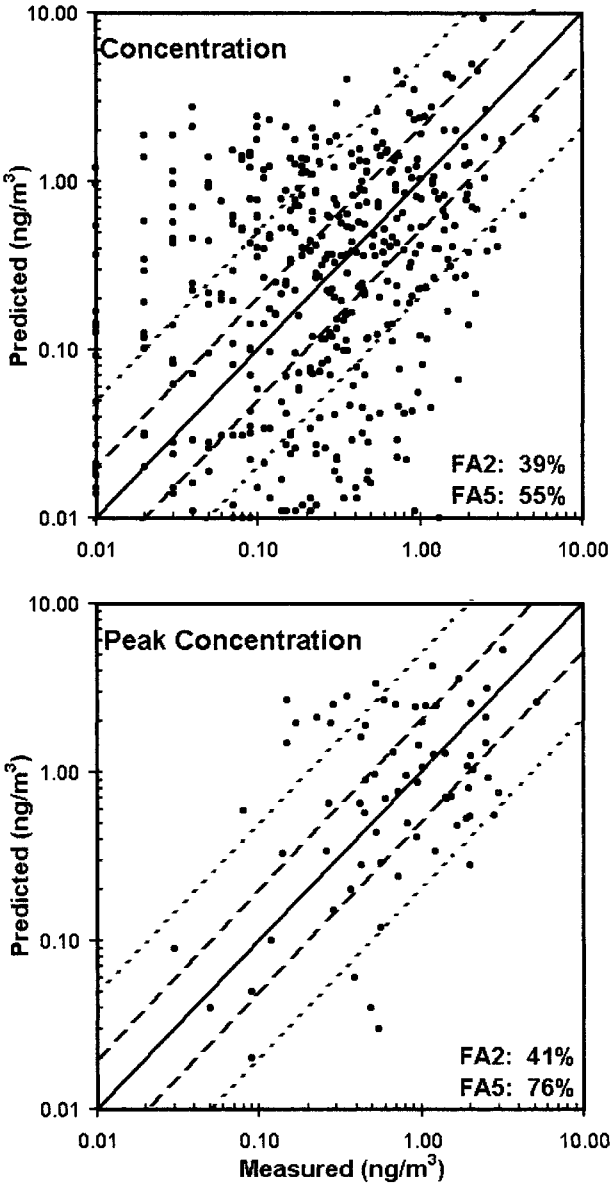


FIG. 10. Scatterplot of global analysis between measured ($M_i$) and predicted ($P_i$) for all concentration pairs, and peak concentration values for all the concentration sampling stations. The locations of these stations are displayed in Fig. 3.

predictions from measurements; and the Pearson correlation coefficient ($P_{corr}$; cf. Mosca et al. 1998a,b).

Figure 10 shows the scatter diagrams for all measured ($M_i$) versus predicted ($P_i$) concentration pairs and for peak concentration pairs. In these scatter diagrams, the pairs are plotted on a logarithmic scale; thus, in the graph the zeros considered are raised to 0.01 ng $m^{-3}$, representing the lower limit of reliability of the measuring instrument. In these diagrams, FA2 and FA5 values are also calculated for the concentration pairs. The concentration pairs are scattered with both unmatched and matched concentration values. We find that FA2 is 39% and FA5 is 55% for concentration pairs. A number of low-value pairs on only one axis are also seen in Fig. 10; this implies that either the measured or the predicted concentration has near zero value while the other has nonzero value. This may indicate that either the measured or predicted cloud is considerably narrower than the other. In this case, ''narrower'' refers partly to the temporal extent and partly to the spatial extent. That is, the predicted cloud's transit time across the sampling station was shorter and earlier than the observed cloud's transit time, resulting in many concentration pairs in which the predicted cloud station concentration was nearly zero while the observed cloud station concentration was greater than nearly zero. In fact, these very low concentration values cause both the FA2 and FA5 values to be decreased. The predicted peak concentration values show better agreement with the measured values, with 41% of the predicted peak concentration values within a factor of 2 of the measured concentration values and 76% within a factor of 5.

Figure 11 shows the scatter diagrams for the predicted and measured time of arrival, the time of peak concentration, and the duration time of the cloud. In general, the predicted time of arrival of the tracer cloud at all sampling sites shows better agreement than the transit time (duration), which was generally two periods too short. For example, the time of arrival and the time of peak concentration are within 3 h (one period) 73% of the time, whereas the duration of the cloud is within 6 h (two periods) 76% of the time.

The global analysis also consist of the calculation of FOEX, bias, NMSE, and $P_{corr}$. Suppose that $N$ pairs ($M_i$, $P_i$) are plotted in a scatter diagram (cf. Fig. 10). In this diagram, it is possible to evaluate the degree of over- or underprediction. If $N_{(Pi>Mi)}$ is the number of overpredictions, or the number of pairs where $P_i > M_i$, FOEX is then defined as

$$\text{FOEX} = \left[\frac{N_{(P_i>M_i)}}{N} - 0.5\right] \times 100, \qquad (16)$$

where FOEX ranges between −50% and +50%. A FOEX equal to −50% means that all the points are below the 45° $y = x$ line (i.e., all the values are underpredicted) while a FOEX equal to +50% means that all the points are above the $y = x$ line (i.e., all the values are overpredicted). The best value is 0%, meaning that the number of underpredictions equals the number of overpredictions.

The bias is defined as the average difference between paired predictions and measurements:

$$B = \frac{1}{N}\sum_i (P_i - M_i), \qquad (17)$$

where $N$ is the number of pairs ($M_i$, $P_i$). It can be positive or negative and, by depending on its sign, it is an estimation of the general overprediction or underprediction of the model with respect to the measurements.

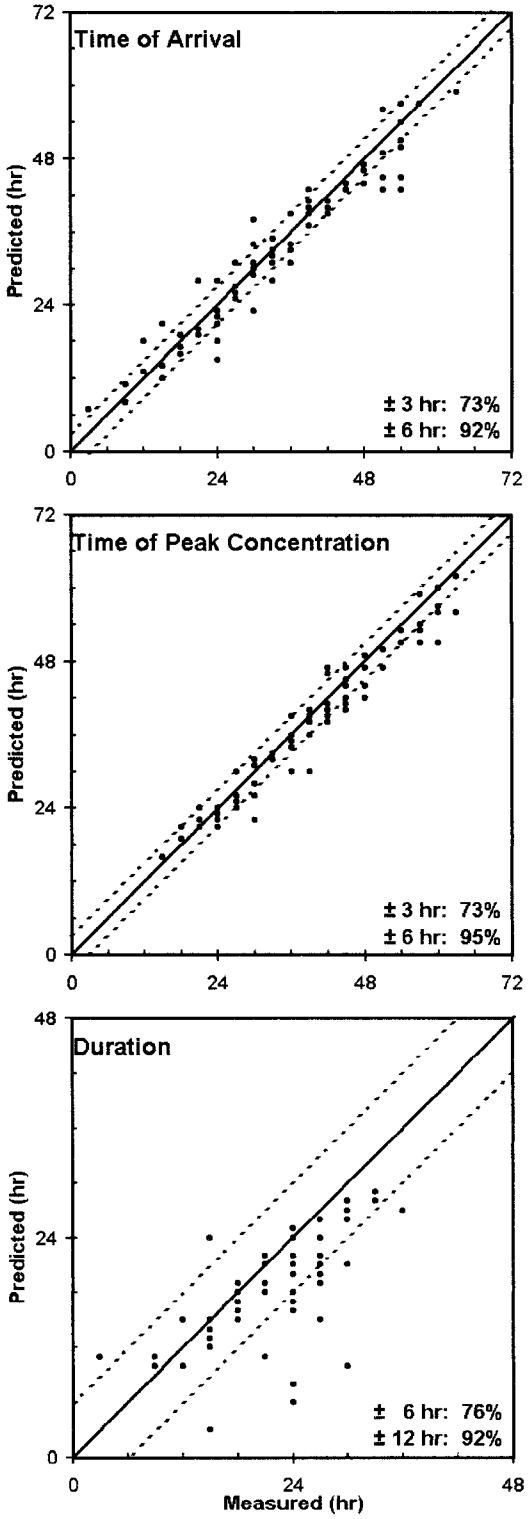


FIG. 11. Scatterplot of time of arrival, time of peak concentration, and duration for all the concentration sampling stations shown in Fig. 3.

Contrary to the FOEX, the bias does not give any information about the number of events of over- or underprediction; it averages the residuals of any couple $(M_i, P_i)$. Thus, a positive value of bias, if alone, can be interpreted in different ways. It might mean that the model overpredicts of a quantity equal to the bias in each point or that it overpredicts in some points and, to a lesser extent, underpredicts in others. Therefore, the classification of an overpredicting (underpredicting) model should be based not only on one coefficient but after an evaluation of several coefficients (e.g., bias, FOEX).

The NMSE is an estimator of the overall deviations between the predicted and measured values. It is defined as

$$\mathrm{NMSE} = \frac{1}{N}\sum_i \frac{(P_i - M_i)^2}{\overline{P}\,\overline{M}}, \tag{18}$$

where $\overline{P} = (1/N)\,\Sigma_i P_i$ and $\overline{M} = (1/N)\,\Sigma_i M_i$. Contrary to the bias, in the NMSE, the squares of the differences are summed instead of the differences themselves. For this reason, the NMSE generally shows the most striking contrast among models. If a model has a very low NMSE, then it is performing well in both space and time. This index gives always positive values, hence it furnishes information on the degree of deviations and not on the partition between over- or underestimations.

The $P_{\mathrm{corr}}$, also called linear correlation coefficient, is given by the formula

$$P_{\mathrm{corr}} = \frac{\sum_i (\ln M_i - \overline{\ln M})(\ln P_i - \overline{\ln P})}{\sqrt{\sum_i (\ln M_i - \overline{\ln M})^2}\sqrt{\sum_i (\ln P_i - \overline{\ln P})^2}}, \tag{19}$$

where $\overline{\ln P} = (1/N)\,\Sigma_i \ln P_i$ and $\overline{\ln M} = (1/N)\,\Sigma_i \ln M_i$. Its value ranges between $-1$ and $+1$. A value of $+1$, the so-called complete positive correlation, corresponds to all the pairs $(M_i, P_i)$ lying on a straight line with positive slope in the scatter diagram. The complete negative correlation corresponds to all the pairs on a straight line with negative slope, and it has a value of $-1$. A value of the Pearson's correlation coefficient near to zero indicates the absence of correlation between the variables. Note that the correlation coefficient is computed on the logarithm of the concentrations because of the wide range of data.

Table 5 summarizes the values of the calculated global statistical measures along with the 12-h FMS values relative to 0.10 ng $m^{-3}$ (presented as dashed line in Fig. 9). The second and third columns in Table 5 show the best and the worst values of the 49 models that participated in the first ETEX release simulation, and the fourth column shows the OMEGA model values. The fifth column compares the OMEGA model performance for all these statistical measures with the performance of the other 49 models. The ranking numbers for OMEGA performance are estimated from the same ranking

TABLE 5. Comparison of OMEGA performance with the 49 models that participated in the first ETEX release simulation (see Mosca et al. 1998a,b).

| | ETEX | | OMEGA | |
|---|---|---|---|---|
| Metric | Best | Worst | Value | Rank |
| FA2 (%) | 42 | 11 | 39 | 4th |
| FA5 (%) | 57 | 25 | 55 | 2nd |
| FOEX (%) | 0 | −42 | −11 | 12th |
| Bias (ng $m^{-3}$) | 0.00 | 1.70 | 0.06 | 7th |
| NMSE (ng $m^{-3}$) | 4.00 | 2644.3 | 6.95 | 8th |
| $P_{corr}$ | 0.71 | 0.04 | 0.58 | 11th |
| 12-h FMS (%) | 50 | 0 | 28 | 9th |
| 24-h FMS (%) | 62 | 3 | 54 | 3rd |
| 36-h FMS (%) | 70 | 0 | 65 | 4th |
| 48-h FMS (%) | 73 | 2 | 70 | 2nd |
| 60-h FMS (%) | 59 | 0 | 39 | 12th |

procedure used during ETEX. In this procedure, statistical indexes of equal values were given the same rank. Note that the statistical values of the other (49) models are reported in Mosca et al. (1998a,b). We must mention here that OMEGA was one of the original 49 models that participated in the first release of the ETEX simulation. At that time (1994), OMEGA was in its very early development stage (OMEGA version 1.0). OMEGA has undergone considerable improvement since then; the results presented in this paper, obtained using OMEGA version 5, are evidence of that improvement.

In general, the OMEGA model results indicate that there are 39% predictions within a factor of 2 around the measurements, and there are 55% predictions within a factor of 5 around the measurements. A FOEX value of −11% indicates that the predictions are nearly equally distributed above and below the measurements with a small tendency to underestimate the concentration values. However, the bias has a value of 0.06, indicating a slight tendency of the model to overestimate the concentration values. This discrepancy indicates that OMEGA gives more underpredicted than overpredicted events, but that the overestimations are higher than underestimations. The NMSE has a values of 6.95 ng $m^{-3}$. This relatively small value indicates that there is a limited spreading of the predictions around the measurements. The $P_{corr}$ has a value of 0.58, indicating a rather good correlation between the measurements and predictions. The 12-h FMS values for 0.10 ng $m^{-3}$ range from 28% to 71% for the five examined times, with maximum values in the central times.

### 3) TIME ANALYSIS

Time analysis of the individual stations is also an important element of evaluating the congruence between the measured and predicted temporal trends of the cloud. Figure 12 presents the time history of the predicted and measured concentrations at six selected sampling sta-

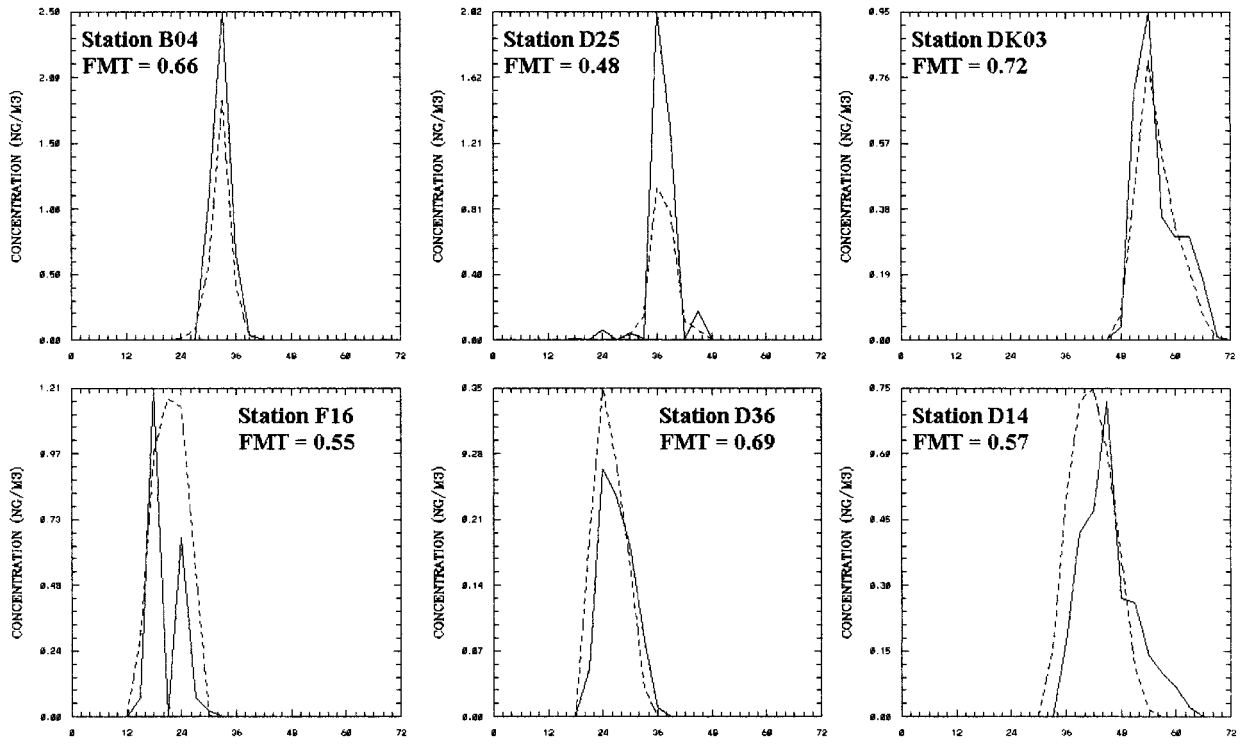


FIG. 12. Time series at stations B04 and F16 in (left) the closest arc, at stations D25 and D36 in (middle) the middle arc, and at stations DK03 and D14 in (right) the farthest arc. The solid line is the measured concentration value; the dashed line is the OMEGA/ADM-predicted concentration value. The locations of these stations are presented in Fig. 3.

tions. These six sampling stations, whose locations are shown in Fig. 3, were selected on three approximate arcs at different distances from the source. The closest arc is located at a distance of approximately 800 km from the source and includes stations B04 and F16. The second arc, including stations D25 and D36, is at a distance of about 1200 km from the source. The third arc includes stations D14 and DK03 and is located at a distance of about 1800 km from the source.

The figure of merit in time (FMT) was also calculated at these fixed locations ($\overline{x}$), for a time series of data. The FMT (Mosca et al. 1998a,b) is defined as:

$$\mathrm{FMT}(\overline{x}) = \frac{\sum_i \min[M(\overline{x}, t_i), P(\overline{x}, t_i)]}{\sum_i \max[M(\overline{x}, t_i), P(\overline{x}, t_i)]}, \qquad (20)$$

where $M$ denotes measured concentration values, and $P$ denotes predicted concentration values. The FMT values can be seen as a statistical coefficient of the time analysis. Analogous to the FMS, the FMT evaluates at a given location the overlap concentration histograms normalized to the time series of the maximum measured or predicted concentration at each time interval. Note that a temporal shift of the time series can significantly reduce the FMT, even if the predicted duration and concentration values are in good agreement with the measurement. Also, a difference between predicted and measured values can give a small FMT, even if time of arrival and duration are correctly predicted. The FMT values for the selected six stations range from 48% to 72%.

## 6. Conclusions

In this study, the OMEGA model was evaluated against the first ETEX experiment by simulating both the weather and the long-range dispersion of inert tracer gas. The OMEGA model was operated in a forecast mode, using only data that were available at the beginning of the simulation period. The OMEGA-predicted meteorological and dispersion fields were compared with the meteorological and dispersion observations both qualitatively and quantitatively. The comparison of the OMEGA results with the ETEX measurements shows good agreement in both the meteorological and the dispersion forecasts.

In general, the OMEGA dispersion results indicated a good agreement in the position, shape, and extension of the tracer cloud. However, differences occurred in cloud shape and duration time, particularly 48 h after the start of the release. The model quantitative comparison with the measurements indicated a good correlation between the measurements and predictions with a limited spreading of the predictions around the measurements. There were 39% of predictions within a factor of 2 around the measurements, while there were 55% of predictions within a factor of 5 around the measurements. The predictions were nearly equally distributed above and below the measurements, with a small tendency to underestimate the concentration values. However, the model results also indicated a slight positive bias (tendency of the model to overestimation of the concentration values). This discrepancy indicated that OMEGA predicted more underpredicted than overpredicted events, but that the overestimations are higher than underestimations.

*Acknowledgments.* This work was supported by the Defense Threat Reduction Agency under contract DTRA01-99-C-0027. The authors thank our program manager Dr. Richard Gustafson for his support. The authors also thank Dr. Ray Hosker of the National Oceanographic and Atmospheric Administration and Dr. John Nasstrom of the Lawrence Livermore National Laboratory for their helpful comments on this manuscript. The authors also thank Mr. C. Agritellis, Dr. S. G. Gopalakrishnan, Dr. Y. Jin, Dr. R. Madala, Mr. D. E. Mays, and Mr. M. D. Turner for their contributions to this work.

## REFERENCES

Anthes, R. A., 1977: A cumulus parameterization scheme utilizing a one-dimensional cloud model. *Mon. Wea. Rev.*, **105,** 270–286.

Bacon, D. P., Z. Boybeyi, P. Boris, T. J. Dunn, M. Hall, R. A. Sarma, S. Young, and J. W. Zack, 1996: An overview of the Operational Multiscale Environment Model with Grid Adaptivity. Preprints, *15th Conf. on Weather Analysis and Forecasting,* Norfolk, VA, Amer. Meteor. Soc., 20–23.

——, and Coauthors, 2000: A dynamically adapting weather and dispersion model: The Operational Multiscale Environment Model with Grid Adaptivity (OMEGA). *Mon. Wea. Rev.,* **128,** 2044–2076.

Beljaars, A. C. M., and A. A. M. Holtslag, 1991: Flux parameterization over land surfaces for atmospheric models. *J. Appl. Meteor.*, **30,** 327–341.

Boybeyi, Z., S. Raman, and P. Zannetti, 1995: A numerical investigation of the possible role of local meteorology in the Bhopal gas accident. *Atmos. Environ.,* **29,** 479–496.

——, D. P. Bacon, P. Boris, T. J. Dunn, M. Hall, R. A. Sarma, S. Young, and J. W. Zack, 1996: System aspects of the Operational Multiscale Environment Model with Grid Adaptivity. Preprints, *11th Conf. on Numerical Weather Prediction,* Norfolk, VA, Amer. Meteor. Soc., 384–385.

Brost, R. A., P. L. Haagenson, and Y.-H. Kuo, 1988: Eulerian simulation of tracer distribution during CAPTEX. *J. Appl. Meteor.,* **27,** 579–593.

Byun, D. W., and J. K. S. Ching, Eds.,1999: Science algorithms of the EPA Models-3 Community Multiscale Air Quality (CMAQ) modeling system. EPA Rep. EPA/600/R-99/030, 750 pp. [Available from National Exposure Research Laboratory, U.S. Environmental Protection Agency, Research Triangle Park, NC 27711.]

Clements, W. E., J. A. Archuleta, and P. H. Gudiksen, 1989: Experimental design of the 1984 ASCOT field study. *J. Appl. Meteor.,* **28,** 405–413.

Draxler, R. R., and J. L. Heffter, 1989: Across North America Tracer Experiment (ANATEX). Volume I: Description, ground-level sampling at primary sites, and meteorology. NOAA Tech. Memo. ERL ARL-167, 83 pp.

Emberlin, J. C., 1981: A sulfur hexafluoride tracer experiment from

a tall stack over complex topography in a coastal area of southern England. *Atmos. Environ.,* **15,** 1523–1530.

Ferber, G. J., K. Telegades, J. L. Heffter, C. R. Dickson, R. N. Dietz, and P. W. Krey, 1981: Demonstration of a long-range atmospheric tracer system using perfluorocarbons. NOAA Tech. Memo. ERL ARL-101, 74 pp.

——, J. L. Heffter, R. R. Draxler, R. J. Lagomarsino, F. L. Thomas, R. N. Dietz, and C. M. Benkovitz, 1986: Cross-Appalachian Tracer Experiment (CAPTEX '83) final report. NOAA Tech. Memo. ERL ARL-142, 60 pp.

Girardi, F., G. Graziani, G. Klug, and K. Nodop, 1997: The European Tracer Experiment description and summary of the ETEX project. *Proc. ETEX Symp. on Long-Range Atmospheric Transport, Model Verification and Emergency Response,* Vienna, Austria, European Commission JRC, International Atomic Energy Agency, and WMO, 83–86.

Glaab H., B. Fay, and I. Jacobsen, 1998: Evaluation of the emergency dispersion model at the Deutscher Wetterdienst using ETEX data. *Atmos. Environ.,* **32,** 4359–4366.

Graziani, G., W. Klug, and S. Mosca, 1998: Real-time long-range dispersion model evaluation of ETEX first release. Office for Official Publications of the European Communities Tech. Rep. EUR 17754 EN, 213 pp.

Heffter, J. L., J. F. Schubert, and G. A. Mead, 1984: Atlantic Coast Unique Regional Atmospheric Tracer Experiment (ACURATE). NOAA Tech. Memo. ERL ARL-130, 15 pp.

Kuo, H. L., 1965: On formation and intensification of tropical cyclones through latent heat release by cumulus convection. *J. Atmos. Sci.,* **22,** 40–63.

——, 1974: Further studies of the parameterization of the influence of cumulus on large-scale flow. *J. Atmos. Sci.,* **31,** 1232–1240.

Lamb, B. K., A. Lorenzen, and F. H. Shair, 1978: Atmospheric dispersion and transport within coastal regions—Part I: Tracer study of power plant emissions from the Oxnard Plain. *Atmos. Environ.,* **12,** 2089–2100.

Langer J., L. Robertson, C. Persson, and A. Ullerstig, 1998: Validation of the operational emergency response model at the Swedish Meteorological and Hydrological Institute using data from ETEX and the Chernobyl accident. *Atmos. Environ.,* **32,** 4325–4333.

Lin, Y.-L., R. D. Farley, and H. D. Orville, 1983: Bulk parameterization of the snow field in a cloud model. *J. Climate Appl. Meteor.,* **22,** 1065–1092.

Lorimer, G. S., 1986: The kernel method for air quality modeling: I. Mathematical foundation. *Atmos. Environ.,* **20,** 1447–1453.

Mahrer, Y., and R. A. Pielke, 1977: The effects of topography on the sea and land breezes in a two-dimensional numerical model. *Mon. Wea. Rev.,* **105,** 1151–1162.

Mellor, G. L., and T. Yamada, 1974: A hierarchy of turbulence closure models for planetary boundary layers. *J. Atmos. Sci.,* **31,** 1791–1806.

Moran, M. D., and R. A. Pielke, 1996: Evaluation of a mesoscale atmospheric dispersion modeling system with observations from the 1980 Great Plains mesoscale tracer field experiment. Part II: Dispersion simulations. *J. Appl. Meteor.,* **35,** 308–329.

Mosca, S., R. Bianconi, R. Bellasio, G. Graziani, and W. Klug, 1998a: ATMES II—Evaluation of long-range dispersion models using data of the 1st ETEX release. Office for Official Publications of the European Communities Tech. Rep. EUR 17756 EN, 459 pp.

——, G. Graziani, W. Klug, R. Bellasio, and R. Bianconi, 1998b: A statistical methodology for the evaluation of long-range dispersion models: An application to the ETEX exercise. *Atmos. Environ.,* **32,** 4302–4324.

Nasstrom, J. S., and J. C. Pace, 1998: Evaluation of the effect of meteorological data resolution on Lagrangian particle dispersion simulations using the ETEX experiment. *Atmos. Environ.,* **32,** 4187–4194.

Nodop, K., R. Connolly, and F. Girardi, 1998: The field campaigns of the European Tracer Experiment (ETEX): Overview and results. *Atmos. Environ.,* **32,** 4095–4108.

Noilhan, J., and S. Planton, 1989: A simple parameterization of land surface processes for meteorological models. *Mon. Wea. Rev.,* **117,** 536–549.

Ryall, D. B., and R. H. Maryon, 1998: Validation of the UK Met. Office's NAME model against the ETEX dataset. *Atmos. Environ.,* **32,** 4265–4276.

Sarma, A., N. Ahmad, D. P. Bacon, Z. Boybeyi, T. Dunn, M. Hall, and P. C. S. Lee, 1999: Application of adaptive grid refinement to plume modeling. *Air Pollution VII,* C. A. A. Brebbia, et al., Eds., WIT Press, 59–68.

Sasamori, T., 1972: A linear harmonic analysis of atmospheric motion with radiative dissipation. *J. Meteor. Soc. Japan,* **50,** 505–518.

Smolarkiewicz, P. K., 1984: A fully multidimensional positive definite advection transport algorithm with small implicit diffusion. *J. Comput. Phys.,* **54,** 325–362.

Sullivan, T. J., J. S. Ellis, C. S. Foster, K. T. Foster, R. L. Baskett, J. S. Nasstrom, and W. W. Schalk III, 1993: Atmospheric release advisory capability: Real-time modeling of airborne hazardous materials. *Bull. Amer. Meteor. Soc.,* **74,** 2343–2361.

Taylor, G. I., 1921: Diffusion by continuous movements. *Proc. London Math. Soc.,* **20,** 196–211.

Uliasz, M., 1990: Development of the mesoscale dispersion modeling system using personal computers. Part I: Models and computer implementation. *Z. Meteor.,* **40,** 110–120.

van Dop H., and Coauthors,1998: ETEX: A European Tracer Experiment; observations, dispersion modeling and emergency response. *Atmos. Environ.,* **32,** 4089–4094.

Webb, R. S., C. E. Rosenzweig, and E. R. Levine, 1992: A global data set of soil particle size properties: Digital raster data on a 1-degree geographic (lat/long) 180 × 360 grid. *Global Ecosystems Database Version 1.0,* NOAA National Geophysical Data Center, Boulder, CO, CD-ROM, disk A.

Yamada, T., and S. Bunker, 1988: Development of a nested grid, second moment turbulence closure model and application to the 1982 ASCOT Brush Creek data simulation. *J. Appl. Meteor.,* **27,** 562–578.

Zannetti, P., 1996: *Computer Methods and Software for Simulating Environmental Pollution and its Adverse Effects.* Vol. 3, *Environmental Modeling,* Computational Mechanics Publications, 462 pp.